MNRAS **458,** 832–844 (2016)
Advance Access publication 2016 February 15
doi:10.1093/mnras/stw331

Hydrodynamic simulations of the interaction between giant stars and planets

Jan E. Staff,[1]★ Orsola De Marco,[1] Peter Wood,[2] Pablo Galaviz[1] and Jean-Claude Passy[3]

[1] *Department of Physics and Astronomy, Macquarie University, NSW 2109, Australia*
[2] *Research School of Astronomy and Astrophysics, Australian National University, Cotter Road, Weston Creek, ACT 2611, Australia*
[3] *Argelander Institut für Astronomie, D-53121 Bonn, Germany*

Accepted 2016 February 8. Received 2016 February 8; in original form 2015 September 7

ABSTRACT

We present the results of hydrodynamic simulations of the interaction between a 10 Jupiter mass planet and a red or asymptotic giant branch stars, both with a zero-age main sequence mass of 3.5 $M_\odot$. Dynamic in-spiral time-scales are of the order of few years and a few decades for the red and asymptotic giant branch stars, respectively. The planets will eventually be destroyed at a separation from the core of the giants smaller than the resolution of our simulations, either through evaporation or tidal disruption. As the planets in-spiral, the giant stars' envelopes are somewhat puffed up. Based on relatively long time-scales and even considering the fact that further in-spiral should take place before the planets are destroyed, we predict that the merger would be difficult to observe, with only a relatively small, slow brightening. Very little mass is unbound in the process. These conclusions may change if the planet's orbit enhances the star's main pulsation modes. Based on the angular momentum transfer, we also suspect that this star–planet interaction may be unable to lead to large-scale outflows via the rotation-mediated dynamo effect of Nordhaus and Blackman. Detectable pollution from the destroyed planets would only result for the lightest, lowest metallicity stars. We furthermore find that in both simulations the planets move through the outer stellar envelopes at Mach-3 to Mach-5, reaching Mach-1 towards the end of the simulations. The gravitational drag force decreases and the in-spiral slows down at the sonic transition, as predicted analytically.

Key words: hydrodynamics – methods: numerical – planet–star interactions – stars: AGB and post-AGB.

1 INTRODUCTION

An increasing number of planets is being discovered at intermediate distances from their host stars (Udry & Santos 2007). Villaver & Livio (2009), Mustill & Villaver (2012) and Nordhaus & Spiegel (2013) among others calculated that expanding giants, whether red giant branch (RGB) stars or asymptotic giant branch (AGB) stars could engulf planets orbiting 2–4 times the maximum radius attained by the star. Such an interaction would likely result in the destruction of the planet producing an observational signature as well as long-lasting and observable evolutionary effects on stars.

Observational clues of star–planet interactions are in the form of putative planets discovered around post-main-sequence stars, close enough that an interaction must have taken place when the star was in its giant phase in the recent past. Examples are the 1.25 M_J planet (where M_J is the mass of Jupiter) orbiting 0.116 au from a horizontal branch star (Setiawan et al. 2010), two Earth-sized objects orbiting a subdwarf B star at a separation of 0.0060 and 0.0076 au (Charpinet et al. 2011), or three Earth-sized planets orbiting a subdwarf B pulsator (Silvotti et al. 2014). These planets must have been engulfed in the envelope of the giant star that became the subdwarf star today. Charpinet et al. (2011) and Passy, Mac Low & De Marco (2012b) showed how planets may have been much more massive initially and lost much of their mass in the common envelope (CE) phase. However, they could not determine how the core of the planets survived the interaction instead of plunging into the core of the giant.

A second type of planet around post-giant stars consists of one or more planets detected at au-distance from post-CE binaries, rather than single stars. Some of those findings have been debated because the planets would not be in stable orbits (Horner et al. 2013) or the data could be as easily explained with alternative, non-planet scenarios. However, other data are more convincingly, though not conclusively, explained by the presence of planetary systems (e.g. NN Serpentis; Parsons et al. 2014). These planets, contrary to the

---

★E-mail: jstaff@ufl.edu

Published by Oxford University Press on behalf of the Royal Astronomical Society

planets at sub-au orbital separations from *single* post-giant stars, are unlikely to have been involved in the CE that created today's close binary, but they must have been impacted by the ejection of the giant's envelope. It has been speculated that they may have formed in the aftermath of the CE binary interaction (Beuermann et al. 2011), similarly to how the planets around pulsar PSR1257+12 (Wolszczan & Frail 1992) were formed after the supernova explosion.

Theoretically Soker (1998) suggested that star–planet interactions could generate blue horizontal branch stars by enhancing the RGB mass-loss rate and decreasing the envelope mass of the red giant star. Carlberg, Majewski & Arras (2009) calculated instead the extent to which interactions (tidal interactions and/or mergers) between giants and planets would spin-up giants. Nelemans & Tauris (1998) found that companions with masses more than 20–25 $M_{\rm J}$ could survive a CE with a 1 $\mathrm{M}_{\odot}$ red giant and expel the envelope. On the other hand, using the formalism from Nelemans & Tauris (1998) and Villaver & Livio (2007) found that companions less massive than $120 M_{\rm J} = 0.11\,\mathrm{M}_{\odot}$ would evaporate inside the envelope of a 5 $\mathrm{M}_{\odot}$ AGB star. Both these studies rely on the uncertain and highly debated efficiency of the CE ejection formalism (De Marco et al. 2011).

Nordhaus & Blackman (2006) investigated analytically 3 $\mathrm{M}_{\odot}$ RGB and AGB stars interacting with a low-mass companion (planet, brown dwarf, or low-mass main-sequence star). They found that envelope ejection in the RGB case is unlikely, but possible for AGB stars from low-mass main-sequence stars. While planets may have too low a mass to eject the AGB star's envelope, they found that a planet may induce differential rotation mediated dynamo that can eject material. Furthermore, the planet may tidally disrupt, creating a disc inside the envelope that can lead to a disc-driven outflow. Metzger, Giannios & Spiegel (2012) investigated mergers between hot Jupiters and their host main-sequence stars and predicted that prior to merger, as the planet penetrates the star's atmosphere, an extreme UV (EUV)/X-ray transient is produced in the hot wake following the planet. The merger would also drive an outflow and hydrogen recombination in the outflow would cause an optical transient. They argued that the Galactic rate of mergers between hot Jupiters and their host stars should be 0.1–1 yr^{-1} and that should be similar to the rate observed for planets and giant stars.

Despite past efforts, many questions still remain. What is the fate of the planet in the CE interaction? Does it survive, or is it destroyed by ablation or tidal disruption? Whatever the fate of the planet, will the interaction lead to an alteration of the star and its subsequent evolution, such as spin-up, mass-loss, or a change in the surface abundances?

Presumably, once a planet is tidally brought closer to an expanding giant star, the star would fill its Roche lobe and transfer mass to the planet. Since the planet is much less massive than the star, it is likely that the planet would be engulfed by the giant's extended envelope and have a CE interaction (Ivanova et al. 2013). CE interactions are thought to happen also between giants and stellar mass companions (Paczynski 1976) and give rise to compact evolved binaries. CE simulations using a variety of techniques (e.g. Sandquist et al. 1998; Passy et al. 2012a; Ricker & Taam 2012; Nandez, Ivanova & Lombardi 2015; Staff et al. 2016) have a range of uncertainties and shortcomings (e.g. Nandez, Ivanova & Lombardi 2015), but can be used as starting points to determine the nature of star–planet interactions. By running hydrodynamic simulations of the CE interaction between a 10 $M_{\rm J}$ planet and an RGB or an AGB star, we start addressing numerically aspects of the interaction such as the time-scale of the interaction, the final separation or the extent to which the stellar envelope is spun-up.

We also exploit the lightness of the planetary companion relative to the stellar envelope to carry out a study of gravitational drag experienced by a body in a CE simulation (Ricker & Taam 2008). This is much more difficult when the companion is more massive because the gas is stirred considerably and it is difficult to extract some of the quantities needed to carry out the calculation.

We describe the numerical method that we use in Section 2. Then in Section 3, we present our results including an appraisal of how numerical considerations impact our conclusions. In Section 4, we assess the drag forces acting on the planet and we exploit the relative composure of the envelope gas to compare these forces to their analytically derived equivalent. We finally discuss our results in Section 5.

2 METHOD

We used a modified version of the grid-based hydrodynamics code ENZO (O'Shea et al. 2004; Passy et al. 2012a; Bryan et al. 2014) to run the hydrodynamics simulations. The calculations were performed on a 256^3 grid in the adiabatic approximation with outflow boundary conditions. In addition, we also performed the same simulations on a grid with 512^3 resolution, to test if the resolution affects the results.

The structure of the giant stars were calculated using the stellar evolution code Modules for Experiments in Stellar Astrophysics (MESA; Paxton et al. 2011, 2013). We used two stellar structures, evolved from the same 3.5 $\mathrm{M}_{\odot}$, zero-age main sequence, solar metallicity model. The first stellar structure was that of the model 283 million years after joining the zero-age main sequence. At this time the star had reached the RGB, having lost 0.01 $\mathrm{M}_{\odot}$. It had a radius of 55 $\mathrm{R}_{\odot}$ (approximately the maximum radius that this type of star reaches on the RGB), a luminosity of 680 $\mathrm{L}_{\odot}$, and an effective temperature of 3960 K.

The second stellar structure was taken 330 million years after the zero-age main sequence. At this time the star had reached the thermally pulsating AGB, had a mass of 3.05 $\mathrm{M}_{\odot}$ a radius of 470 $\mathrm{R}_{\odot}$, a luminosity of $1.4 \times 10^4\,\mathrm{L}_{\odot}$ and an effective temperature of 2920 K (the structure was taken between two thermal pulses). This is the same stellar structure used for the simulations of Staff et al. (2016). Stars more massive than $\sim 2\,\mathrm{M}_{\odot}$ grow a lot larger on the AGB than on the RGB, providing for an opportunity for planets that had not interacted on the RGB to do so during the AGB. This is the reason why we chose to use a star more massive than 2 $\mathrm{M}_{\odot}$. Stars less massive than approximately 2 $\mathrm{M}_{\odot}$ have similar maximum RGB and AGB radii and this means that they have most of their interactions on the RGB. For the more luminous low-mass ($M < 2\,\mathrm{M}_{\odot}$) RGB stars, which can attain radii close to 200 $\mathrm{R}_{\odot}$, the nature of the star–planet interaction will be intermediate between the RGB and AGB cases considered here.

We mapped the 1D MESA model into the ENZO computational domain. MESA models have much higher resolution compared to the linear resolution of the 3D Cartesian ENZO grid that we use. The size of the simulation box used for the simulation with the smaller RGB star was 3×10^{13} cm (2 au), such that each cell in 256^3 cell domain had a size of 1.2×10^{11} cm (1.7 $\mathrm{R}_{\odot}$). In the simulation with the larger AGB star, the simulation box was 2.2×10^{14} cm (15 au), and each cell in 256^3 resolution had a size of 8.6×10^{11} cm (12 $\mathrm{R}_{\odot}$). The cell size was half these values for the 512^3 resolution simulation. The cores of the giant stars, where much mass is concentrated, as well as the planet companion cannot be resolved. Instead, they are approximated by point masses, with a smoothed gravitational potential as discussed in Passy et al. (2012a) and by Staff et al. (2016). We used a smoothing length of 3 cells, instead of 1.5, which, as was discussed in Staff et al. (2016), results in better energy conservation.

MESA takes microphysics into account, while we use an ideal gas equation of state with an adiabatic pressure–density relation ($\gamma = 5/3$) in ENZO. Because of this and the addition of a point mass with a smoothed gravitational potential, the star is not in perfect hydrostatic equilibrium in ENZO. Following the method described by Passy et al. (2012a), we force the starting model to hydrostatic equilibrium by dampening the velocities by a factor of 3 for each time step after mapping the stellar structures into the computational domain. We then check the stability by running the simulations without damping the velocities for 4 dynamical times (the dynamical times are 0.07 and 1.8 yr for the RGB and AGB stars, respectively). The simulation volume not occupied by stellar gas is filled with a hot medium, which has a density four orders of magnitude lower than the giant star's least dense point and a high temperature so as to balance the pressure at the surface of the giant star. Despite this, the outer layers of the star tend to diffuse out somewhat (see Staff et al. 2016). The 3D star constructed in this way tends to be slightly larger than it was initially. For both models, the post-stabilization radius was ≈5 per cent larger (2.5 and 23 $\mathrm{R}_\odot$ larger for the RGB and AGB models, respectively, at a density one order of magnitude less than the initial lowest density in the star).

Once the giant star is stabilized, we insert a planet with a mass of $10\,M_\mathrm{J}$ at 1.1 times the radius of the MESA model (R_star), in a circular orbit. In both simulations this initial configuration results in the giant stars massively overflowing their Roche lobe radii. This is the case with many CE simulations (e.g. Sandquist et al. 1998; Passy et al. 2012a) and may have some effect on the CE outcome (Iaconi et al. in preparation). However, in the case of planetary companions, it is likely that the effect of starting close to the surface is minimal: companions as far as 2–3 stellar radii are likely to be captured (Villaver & Livio 2009; Mustill & Villaver 2012), but the angular momentum of the orbit transferred to the primary would confer to it only a relatively minor surface velocity of 1.1–1.3 $\mathrm{km\,s^{-1}}$ for the AGB star and 3.2–3.9 $\mathrm{km\,s^{-1}}$ for the RGB star (this range was found assuming that all the orbital angular momentum of the planet at a distance of 2–3 stellar radii is transferred to the envelope of the giant, and that this envelope rotates rigidly), not too different from our non-rotating initial models.

3 RESULTS: THE IN-SPIRAL

With our starting conditions ($a_0 = 1.1\,R_\mathrm{star} = 61\,\mathrm{R}_\odot = 0.28$ au, and an orbital period of 26 d for the RGB star and $a_0 = 1.1\,R_\mathrm{star} = 520\,\mathrm{R}_\odot = 2.4$ au and an initial period of 1.9 yr for the AGB star), the planet is rapidly engulfed by stellar envelope gas. We show the evolution of the density for the RGB star in Fig. 1 and for the AGB star in Fig. 2. As the planet in-spirals, the giant star's envelope expands. This puffed-up envelope has typical densities of $\sim 10^{-10}\,\mathrm{g\,cm^{-3}}$ in the RGB simulation and $\sim 10^{-12}\,\mathrm{g\,cm^{-3}}$ in the AGB simulation. As the stellar envelope is puffed-up due to the interaction, the photosphere is likely to be located near the edge of this expanding gas. Due to the high-temperature ambient medium, this low-density puffed-up gas may be artificially heated. Therefore we cannot accurately determine the temperature of the photosphere, nor how fast it would cool off radiatively and therefore recede. Especially in the RGB simulation, where the interaction is

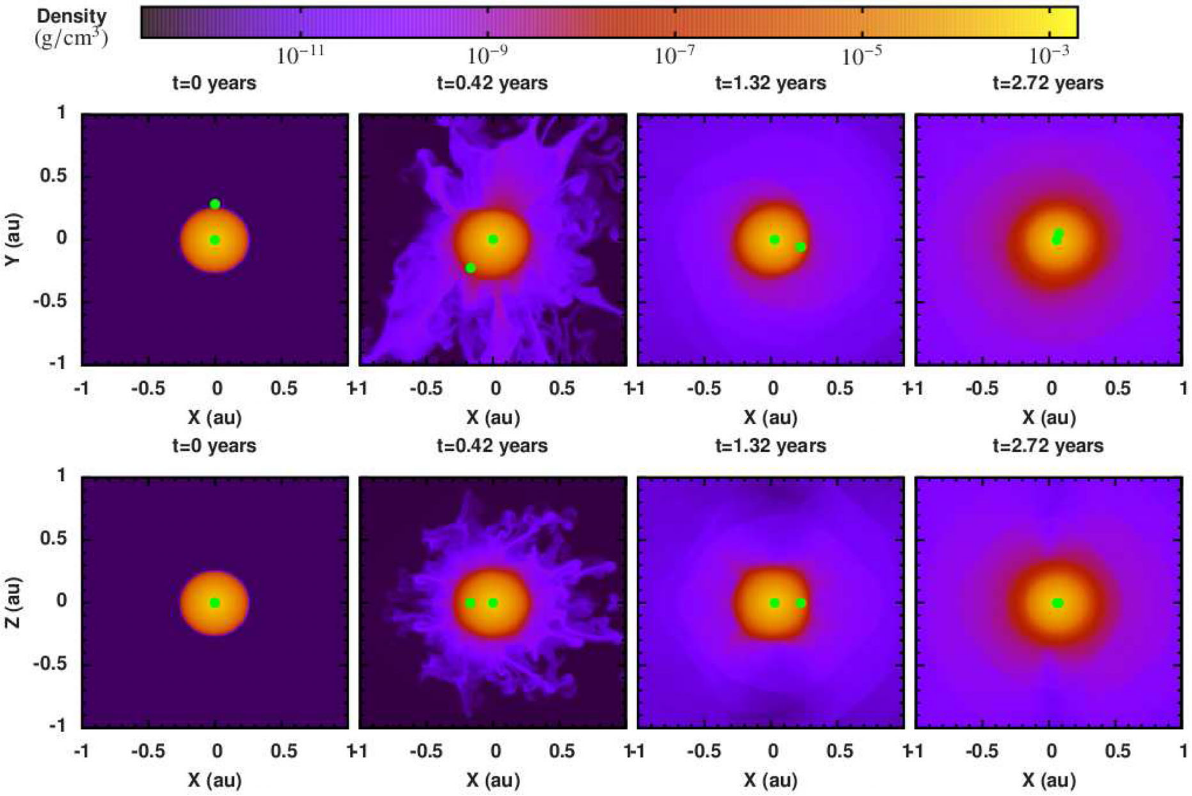

Figure 1. Density slices taken through the middle of the grid on the perpendicular (upper panels) and orbital (lower panels) planes, at four different times, for the low-resolution simulation with the RGB star. The leftmost column shows the initial setup. The core of the RGB star and the planet are indicated by green dots.

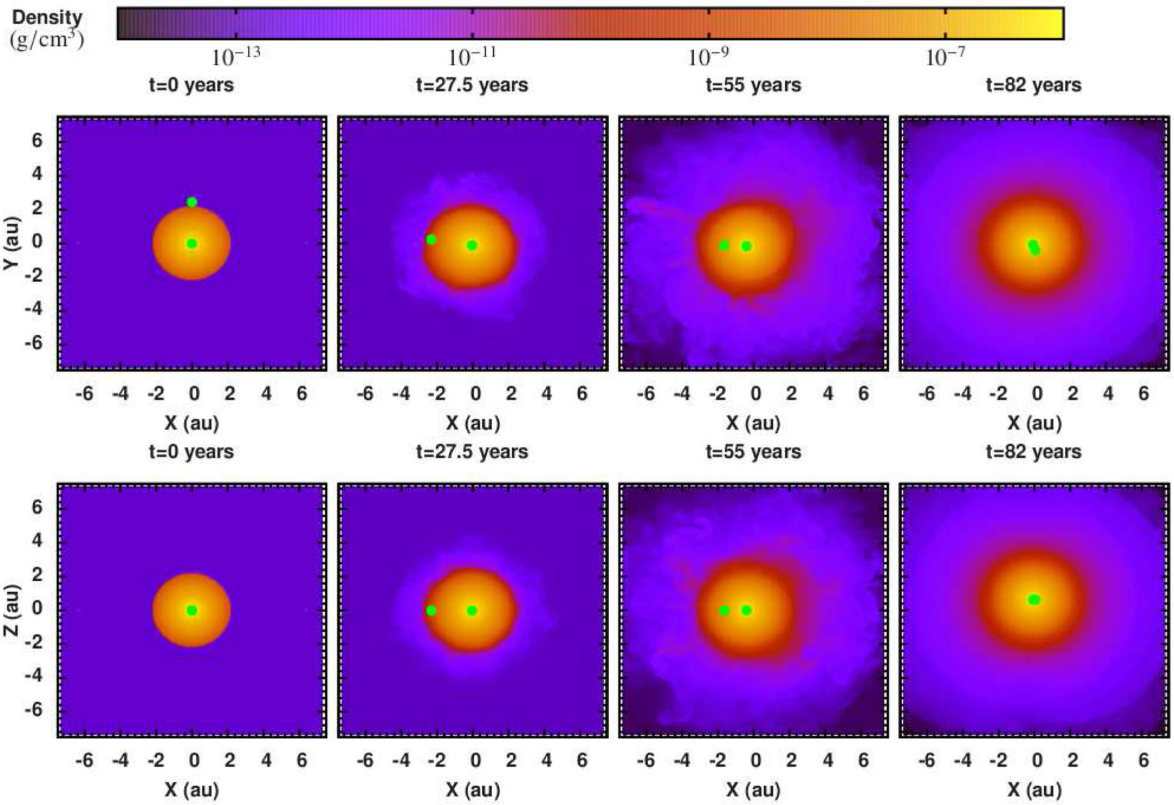

Figure 2. Density slices taken through the middle of the grid on the perpendicular (upper panel) and orbital (lower panel) planes, at four different times, for the low-resolution simulation with an AGB star and a planet. The leftmost column of panels is the initial setup in the three different cuts, then at $t = 27.5$, 55 and 82 yr. The core of the RGB star and the planet are indicated with green dots.

reasonably quick, it seems likely that a significant increase in the photospheric radius could be achieved.

Some low-density gas is lost from the domain, $\lesssim 0.01\,\mathrm{M}_\odot$ in both simulations. Of the mass lost from the simulation box, $\lesssim$10 per cent ($\approx 10^{-3}\,\mathrm{M}_\odot \approx 1\,M_\mathrm{J}$) is unbound in the RGB simulation, and $\lesssim$30 per cent ($\approx 3 \times 10^{-3}\,\mathrm{M}_\odot \approx 3\,M_\mathrm{J}$) is unbound in the AGB simulation (see Fig. 3). We note that initially, a larger amount of the ambient medium is unbound in the AGB simulation compared with the RGB simulation, which in part explains why the AGB simulation unbinds more mass. Pre-empting our discussion on energy conservation in Section 3.1, we note that there is considerable uncertainty on the mass unbinding. The change in the planet's orbital energy as it spirals through the RGB star layers, that can lead to unbinding of envelope, is $\sim 3 \times 10^{45}$ erg, an order of magnitude smaller than the artificial growth in the total energy in the box for that simulation. This artificial growth in energy may therefore be the main driver for the meagre mass unbinding observed, making our estimate for the RGB case an upper limit.

Shown in Fig. 4 are a series of quantities, which we describe and compare in detail below, for both low and high resolution, RGB and the AGB simulations. In the top panel, we show the separation between the planet and the core of the giant star as a function of time, then we show the planet's Mach number (M_p) as it moves through the stellar envelope; third is its velocity with respect to the Keplerian value (v_Kep), then its velocity with respect to the grid, followed by the envelope density surrounding the planet, and, finally, the gravitational drag force acting on the planet in the low-resolution simulation (sixth panel) and the high-resolution simulation (seventh or bottom panel). The last two panel rows will be exhaustively discussed in Section 4. The sound speed used to compute the Mach number is just the sound speed in the cell in which the particle is located. Likewise, the density and velocity of the gas surrounding the particle are the values of the cell where the particle is located.

The overall behaviour of the separation is a gradual decrease over 2–3 yr in the RGB simulation, and over approximately 60–80 yr in the AGB simulation (faster for the higher resolution simulations), after which we cannot follow the evolution because the separation approaches 0.05 and 0.4 au for the RGB and AGB simulations, respectively, which is close to two smoothing lengths (one smoothing length in the lower resolution simulations is 3.5×10^{11} cm = 0.023 au for the RGB star and 2.6×10^{12} cm = 0.17 au for the AGB star), at which point the smoothing of the potential may begin to impact the results (see also Section 3.1).

The oscillatory behaviour seen in the separation plot for the low-resolution RGB star in Fig. 4 has a period of ≈25 d (similar to the planet's initial orbital period) and is due to the development of an eccentricity, typically observed during the fast in-spiral phase of CE simulations and ascribed to the non-symmetric distribution of gas (see e.g. Passy et al. 2012a). Between ∼100 and ∼300 d in the RGB simulation, the orbital separation and the planet's velocity remain approximately constant. Following this, the planet speeds up as the separation decays. In the higher resolution RGB simulation, the snapshots from the hydrodynamics simulation were produced less frequently, with a frequency of 0.1 yr (which is larger than the oscillatory period), and this oscillatory behaviour is therefore partly hidden in Fig. 4. In the AGB simulation, the separation also remains approximately constant for the first ∼30 yr and the orbit

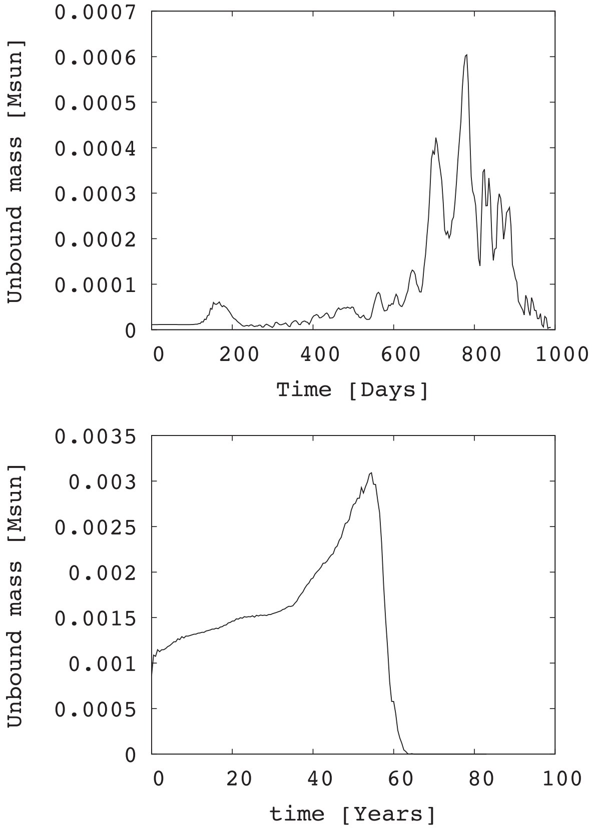

Figure 3. The unbound mass in the computational domain as a function of time for the RGB star (upper panel), and the AGB star (lower panel) orbited by a 10 M_J planet (in both cases the figures are from the low-resolution simulations).

develops a lower eccentricity than for the RGB case. After this, the separation decays, and between 50 and 60 yr there is a rapid decrease in the separation. Although we observe a period of faster in-spiral between 700 and 800 d in the RGB simulation, this is not as prominent as in past CE simulations or in the CE between the planet and the AGB star. It is however similar to the behaviour of a 0.01 $\mathrm{M}_\odot$ companion plunging into the 0.88 $\mathrm{M}_\odot$, 85 $\mathrm{R}_\odot$ RGB star (De Marco et al. 2012).

During the interaction the outer layers of the puffed-up envelope gain rotation. At densities lower than the initial photospheric density ($\rho < 8 \times 10^{-9}$ g cm^{-3} for the RGB star and $\rho < 1 \times 10^{-9}$ g cm^{-3} for the AGB star), rotational velocities of $\gtrsim$20 km s^{-1} are found in the RGB simulation, and $\gtrsim$5 km s^{-1} are found in the AGB simulation (see Fig. 5). But since the planet has a low angular momentum due to its low mass, the planet is unable to noticeably spin-up the higher density, more massive, layers of the giant stars. At higher densities than the photospheric density of the initial model the star is therefore not rotating.

The velocity of this puffed-up envelope is, however, small compared to the planet's velocity around the giant star, and the planet's orbital velocity with respect to the grid is therefore similar to the velocity relative to the surrounding gas in both simulations. The planet's velocity early in the simulation is seen to oscillate between 100 and 120 km s^{-1} in the RGB case, while in the AGB simulation the orbital velocity of the planet varies less around a value of $\approx$35 km s^{-1}. During the fast in-spiral, at approximately 600 d in the RGB simulation, the velocity continues to oscillate and increases up to $\approx$130 km s^{-1}, while in the AGB simulation the velocity is seen to oscillate more towards the end of the simulation, reaching a maximum of $\approx$50 km s^{-1}. As the planet in-spirals, its velocity is found to remain approximately Keplerian throughout both simulations.

Once the planet becomes submerged in the stellar envelope, the Mach number jumps to 4 or 5 in both simulations (see Fig. 4). During the rapid in-spiral phase, the Mach number decreases as the sound speed grows deeper inside the giant stars. At the end of both simulations, the planet's velocity is approximately the same as the sound speed. In Section 4, we will discuss the drag force in relation to the Mach number of the particles.

3.1 Numerical considerations

To test whether the resolution affects our results, we have performed both simulations with a higher resolution of 512^3 cells. The results are qualitatively similar. The main differences are that the orbital separation tends to a lower value in the higher resolution simulation, and that the in-spiral is faster (see Fig. 4). In both cases, following the slow-down in orbital decay, the in-spiral continues at a slower pace until we stop the simulation. We also found that about half as much mass becomes unbound in the higher resolution simulation ($\approx 5 \times 10^{-4}$ $\mathrm{M}_\odot$ versus $\approx 9 \times 10^{-4}$ $\mathrm{M}_\odot$ for the lower resolution RGB simulation), despite the fact that at higher resolution more orbital energy is delivered as the higher resolution allows us to follow the in-spiral further. The star remains somewhat more compact in the higher resolution simulation, which is evident in the steeper increase in V_p as the planet approaches the core, particularly in the RGB simulation. The accretion radius of the planet is not resolved in any of our simulations. We discuss the implications in Section 4.

Our simulations conserve energy reasonably well. We find that the total energy on the grid in the RGB simulation increases by $\approx 3 \times 10^{46}$ erg over the course of the simulation (see Fig. 6). This is $\approx$3 per cent of the initial gravitational potential energy of the gas on the grid, which was $\approx 1 \times 10^{48}$ erg. It is $\sim$10 times the change in the planet's potential energy, and $\sim$100 times the change in the planet's kinetic energy. However, over the same time, 8.8×10^{-3} $\mathrm{M}_\odot$ are lost from the grid. If all this lost mass carried the thermal energy of the initial low-density ambient medium, this mass-loss from the domain would remove 6.6×10^{46} erg from the grid.[1] We therefore estimate that the total energy has increased by up to 9.6×10^{46} erg, corresponding to 10 per cent of the initial potential energy of the star. We compare the energy gained due to non-conservation to the potential energy of the star[2] instead of the total energy in the box. The latter quantity is meaningless, because the total energy in the box can be made arbitrarily high and close to zero by the addition of an arbitrary quantity of hot 'vacuum'.

We also emphasize that 10 per cent is an upper limit to the non-conservation, because most of the mass lost from the grid has a lower thermal energy than the initial hot ambient medium. We find that much of the gas leaving the simulation box has a specific thermal energy of $\sim 10^{13}$ erg g^{-1}. Assuming that this is representative for all the gas leaving the box, we can determine a lower limit to the energy non-conservation. Then $\approx 2 \times 10^{44}$ erg would be lost from the box (i.e. a factor of $\gtrsim$100 less than the above estimate), and hence the energy non-conservation over the course of the simulation would be approximately 3 per cent. In assuming that the gas that leaves

---

[1] The kinetic energy and the gravitational potential energy of the low-density ambient medium are negligible compared to the thermal energy.

[2] The total energy of the star is almost identical to its potential energy, because kinetic and internal components are not very large.

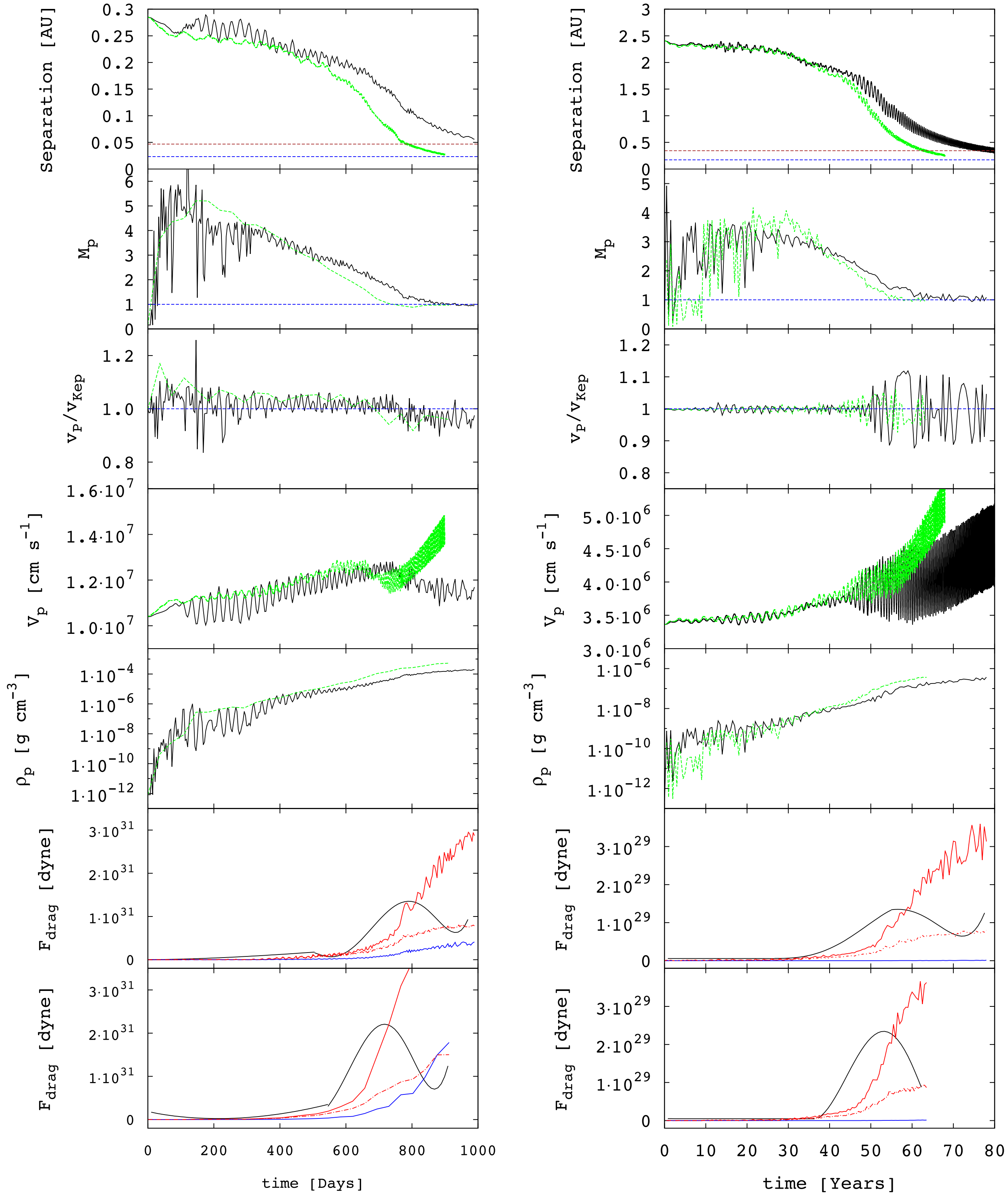

Figure 4. Results from the RGB simulation (left-hand column) and AGB simulation (right-hand column). Black curves are results from the low-resolution simulations. Green curves are from the high-resolution simulations. Upper panel: separation between the core and the planet as a function of time. The blue dashed line represents two smoothing lengths in the higher resolution simulation, while the brown dashed line represents two smoothing lengths in the lower resolution simulation. Second panel: the Mach number of the planet as a function of time. The dashed blue line indicates $M_{\mathrm{p}} = 1$.Third panel: the planet's velocity relative to the Keplerian velocity. The dashed blue line indicates $v_{\mathrm{p}}/v_{\mathrm{Kep}} = 1$. Fourth panel: the planet's velocity relative to the grid. Fifth panel: the density of the stellar envelope around the planet. Sixth panel: the drag force calculated in the low-resolution simulations (black curve), compared with the gravitational drag force calculated from the analytical expression including pressure effects (equation 2; dashed red curve), and excluding pressure effects (solid red curve), as well as the hydrodynamic drag force (blue curve) calculated from the analytical expression (equation 1). Seventh (bottom) panel: the same as the sixth panel, but for the high-resolution simulations.

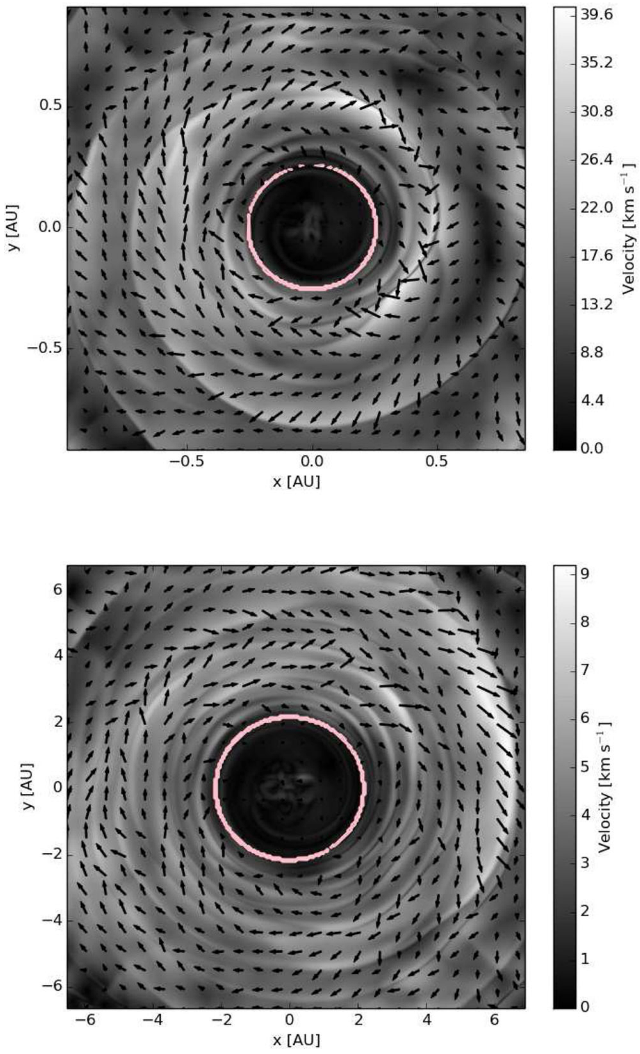

Figure 5. The velocity of the gas in the equatorial plane at the end of the low-resolution simulations. Top panel: RGB star, bottom panel: AGB star. The plotted velocity is $\sqrt{v_x^2 + v_y^2}$, with the arrows showing the direction. The pink circle indicates the size of the giant star prior to the interaction. It is only the puffed-up, low-density matter at larger radii that gains significant rotational velocity, while the high-density interior of the stars have very low rotational velocity.

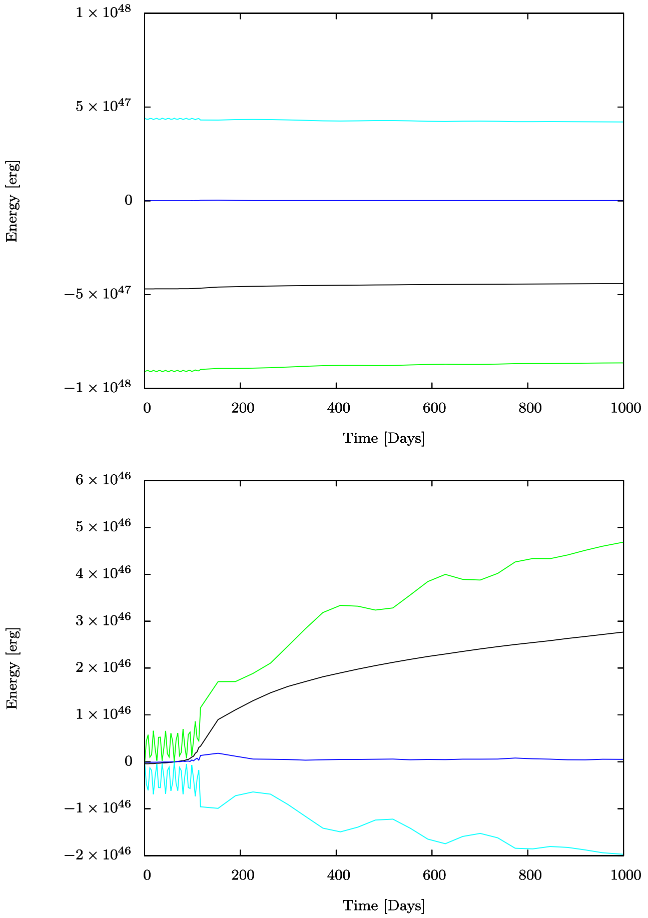

Figure 6. Top panel: energy components on the grid in the lower resolution RGB simulation as a function of time (cyan curve: thermal energy, blue curve: kinetic energy, black curve: total energy and green curve: gravitational potential energy). Bottom panel: the energy components shifted so that the curves start at 0, to illustrate the differences over time.

the box removes 2×10^{44} erg we omitted accounting for its kinetic and potential energies. However, kinetic energy and gravitational potential energy of the stellar envelope material lost from the grid have opposite signs and are of the same order of magnitude as the thermal energy. Hence, it will not significantly change our estimate. Therefore, the energy non-conservation in the RGB simulation is between 3 and 10 per cent, likely closer to 3 per cent. The conservation is slightly better in the higher resolution simulation, but still has a lower limit of roughly 3 per cent.

In the AGB simulation, we find that the total energy decreases by 3×10^{45} erg over 60 yr. However, the total potential energy in the AGB simulation is $\approx 8 \times 10^{46}$ erg, approximately a factor of 10 less than in the RGB simulation, since the AGB star is less tightly bound. The specific thermal energy of the ambient medium is similar to that in the RGB simulation, and therefore the level of non-conservation is even more sensitive to how much thermal energy is carried away by the lost mass. We find that $\sim 1 \times 10^{31}$ g was lost from the grid over the course of the simulation. If all of this mass had a specific thermal energy of $\sim 10^{13}$ erg g^{-1}, we find that the total energy should have dropped $\sim 1 \times 10^{44}$ erg, which is small compared to the actual drop of 3×10^{45} erg. This way, we find that the energy is conserved to within 4 per cent in the AGB simulation. This is, however, an estimate for the energy conservation based on a lower estimate for the energy lost from the grid associated with mass-loss. It is likely that the lost mass has taken out a larger amount of thermal energy, which would make the conservation better, unless the lost mass has removed more than $\sim 6 \times 10^{45}$ erg (corresponding to a specific thermal energy of more than $\sim 6 \times 10^{14}$ erg g^{-1}). We therefore expect the energy to be conserved to within a few per cent also in this simulation.

4 DRAG FORCES

The torque acting on the planet dictates the rate of in-spiral. Determining whether simulations represent the drag forces with sufficient accuracy is an important step when determining whether results of simulations are reliable. Below we consider both gravitational and hydrodynamic drag components and compare what should be going on in nature, expressed by analytical approximations, with what is going on inside the simulation, calculated from the quantities that are output from the code.

4.1 Gravitational versus hydrodynamic drag

In nature, a planet in a CE phase with its host star would experience a drag force composed of gravitational and hydrodynamic components. The hydrodynamic drag force is due to the ram pressure on the planet from the surrounding gas, and this force can be estimated:

$$F_{\rm hydro,drag} \sim \rho v_{\rm p}^2 \pi R_{\rm p}^2, \tag{1}$$

where $v_{\rm p}$ is the planet's relative velocity with respect to the surrounding gas, $R_{\rm p}$ is the radius of the planet, and ρ is the density of the envelope gas surrounding the planet.

The gravitational drag is instead due to gravitational forces between the gas flowing past the planet and the planet itself. Although there is no accurate expression for the gravitational drag in the presence of a density gradient (MacLeod & Ramirez-Ruiz 2015), an approximate expression can be found in Iben & Livio (1993) and Passy et al. (2012a):

$$F_{\rm grav,drag} \sim \zeta \rho v_{\rm p}^2 \pi R_{\rm A}^2, \tag{2}$$

where ζ is a numerical factor that depends on the Mach number (it is larger than 2 for supersonic motion and less than unity for subsonic motion Shima, Matsuda & Sawada 1985), and $R_{\rm A}$ is the accretion radius given by (Iben & Livio 1993):

$$R_{\rm A} = \frac{2\,GM_{\rm p}}{v_{\rm p}^2 + c_{\rm s}^2}, \tag{3}$$

for subsonic and sonic speeds, when pressure effects are included (Bondi 1952). This tends to

$$R_{\rm A} = \frac{2GM_{\rm p}}{v_{\rm p}^2}, \tag{4}$$

for high Mach numbers (Hoyle & Lyttleton 1939). In equation (3), $c_{\rm s}$ is the sound speed. For simplicity we assume $\zeta = 1$ always, which means that we will underestimate the gravitational drag force in the supersonic regime, and overestimate it in the subsonic one.

Our simulations do not reproduce the hydrodynamical drag, because the planet is approximated by a point particle and has no surface. Some hydrodynamic drag may be felt by the planet in the simulations due to the fact that some gas gathers in the potential well of the planet moving with it and in so doing it collides with surrounding gas. However, because of the relatively low mass of the planet, this effect is small in the simulations.

Ricker & Taam (2008) predicted that the hydrodynamic drag should be much weaker than the gravitational drag in CE simulations with stellar mass companions. However, planets have much lower mass and a correspondingly weaker gravitational drag. As we show in Fig. 4, towards the end of the RGB simulation the hydrodynamic drag should be comparable to or even dominate the gravitational drag including pressure effects (which is the relevant gravitational drag force at that time). At this point the simulations misrepresent the force on the planet, and we stop them. This does not happen in the AGB simulations, where the hydrodynamic drag should always be negligible compared to the gravitational drag force.

4.2 A comparison between numerical and analytical expressions of the gravitational drag

In order to compare the analytical estimates of the gravitational drag (equations 2– 4) with the actual gravitational drag experienced by the planet in the simulations, we need to device a way to extract this information from the simulation outputs. We calculate the difference in the planet's energy (kinetic plus gravitational potential energies) between two successive snapshots from the simulation. This difference is due to the gravitational drag force, which does work (W) on the planet. This force is approximately antiparallel with the planet's motion, and its magnitude is therefore given by

$$F_{\rm drag,code} = W/s, \tag{5}$$

where s is the distance travelled by the planet between two snapshots. We estimate s by taking the velocity of the planet at the first snapshot and multiplying it by the time between the snapshots. The resulting drag force is plotted alongside the other relevant quantities in Fig. 7.

This estimate is approximate but reasonably accurate. We checked that this estimate of the force is similar to what would result from determining the orbit-averaged radial position of the planet at each time step, thereby determining the force by calculating the second differential of that radial distance and multiplying by the planet's mass. Another method is to read the total acceleration on the planet from the code output. This method is more noisy because the total value of the acceleration includes the dominating centripetal value, which needs to be subtracted from the total.

The values of the orbital energy of the planet and of its velocity vary between one output frame and the next (see Fig. 7). The planet's total energy decreases but occasionally it grows slightly between two snapshots, which results in a drag force that is instantaneously negative. In addition, the planet's velocity can vary by up to 25 per cent between snapshots for the AGB simulation (see Fig. 7, where we plotted the planet's velocity with respect to the surrounding gas, in contrast to in Fig. 4, where we plotted the planet's velocity relative to the grid).

To eliminate the oscillations we fitted the total energy, as well as the planet's velocity and use the fitted curves to determine the value of the gravitational drag force. The force curve has an upturn at the end of the curve, which is an edge effect inherited by the fit to the planet's velocity (middle panel in Fig. 7). In this figure, we only show values for the lower resolution simulations. More details about the fits are provided in the appendix.

The gravitational drag force values for both the lower and higher resolution simulations calculated with the method we have explained above, are also shown in the bottom two panels of Fig. 4 (black curve), where they are compared to the hydrodynamic drag force (blue curve) from equation (1), and to the analytically derived gravitational drag force (supersonic case: solid red curve, or including pressure effects: dashed red curve). We plot the gravitational drag force both including and excluding pressure effects, because the planet is supersonic until ∼800 d in the lower resolution RGB simulation and ∼55 yr in the lower resolution AGB simulation (see the second panel in Fig. 4).

Both the expressions in equations (1) and (2), depend on the density surrounding the planet and the velocity of the planet with respect to the surrounding gas. These are plotted in the fourth and fifth rows of Fig. 4. Initially, the planet starts just outside the star at 1.1 $R_{\rm star}$, and the density surrounding it is the low ambient background density. However, as the giant star expands, the planet finds itself embedded in higher density material. The few oscillations seen in the density surrounding the planet at ∼200 d in the RGB simulation and ∼20 yr in the AGB simulation are due to the planet acquiring a slight eccentricity, or because the star in our simulations is not entirely spherical at this point in time, and so the planet may encounter different densities even if it is in a circular orbit. As the planet in-spirals through the star's envelope, the density gradually increases, to reach a maximum at the end of the

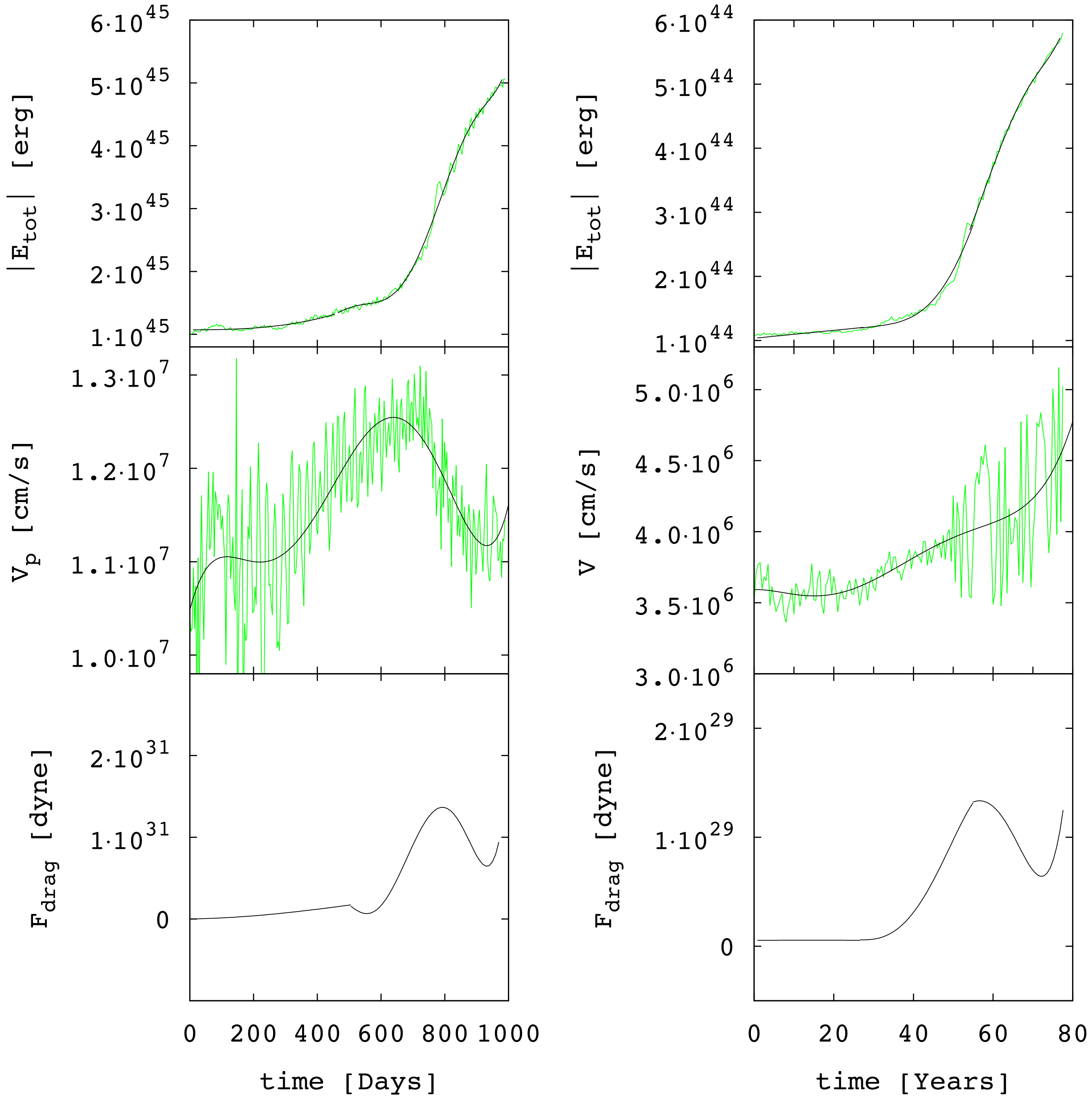

Figure 7. Results from the low-resolution RGB simulation (left-hand column) and AGB simulation (right-hand column). The green curves are the raw data, showing top panel: the absolute value of the planet's total energy, middle panel: the planet's velocity relative to the surrounding gas (in contrast to the velocity relative to the grid shown in Fig. 4). The black curve is a fit to the total energy (top panel) and the velocity (middle panel), and using these fits we have calculated the drag force (bottom panel). This drag force is also shown in Fig. 4.

simulation of $\approx 10^{-4}$ g cm^{-3} after $\sim$1000 d, in the RGB simulation, and $\approx 10^{-6}$ g cm^{-3} after $\sim$80 yr, in the AGB simulation.

The gravitational drag force calculated from the simulations follows closely the pace of the in-spiral from which it is calculated. It increases during the fast in-spiral phase, between 600 and 800 d to ~ 1–2×10^{31} dyne in the RGB simulation, and between 30 and 50 yr to ~ 1–2×10^{29} dyne in the AGB simulation. This leads to an acceleration of the planet due to the drag of approximately -1 cm s^{-2} in the RGB case, and -0.01 cm s^{-2} in the AGB case. The difference in drag force in the RGB and the AGB simulations is primarily due to the different densities encountered by the planet. The peak force in the higher resolution simulations is approximately a factor of 2 larger than in the lower resolution simulations (see Fig. 4).

Looking at the drag forces in the last panel of Fig. 4 – for the high-resolution simulations, we see that the computationally derived force is 2–3 times larger than the analytically calculated *supersonic* gravitational drag force for both RGB (at around 600 d) and AGB (between 40 and 50 yr) simulations, due either to the use of $\zeta = 1$ in equation (4), or to an actual effect of the density gradient exerting an added component to the force (MacLeod &

Ramirez-Ruiz 2015). Following this increase, the drag force then decreases becoming the same as the expression for the gravitational drag including pressure effects at 820 d and 65 yr for the RGB and AGB simulations, respectively. The force values peak when the planet's Mach numbers are slightly larger than unity in both simulations. We interpret this by looking at equation (2) and noticing that in the supersonic regime, $R_{\rm A}$, and the gravitational drag force, can be seen to increase with decreasing velocity (smaller Mach numbers). However, when the force transitions to the sonic case, ζ is smaller, and hence the force decreases. Although a quantitative comparison cannot be carried out, this behaviour is that predicted by Ostriker (1999): the force is largest at, or slightly above the sonic point and drops dramatically just below Mach-1. In these simulations, we conclude this is what causes the sudden decrease in drag force that makes the in-spiral slow down (see Fig. 4).

We finally note that the particle representing the core of the giant also experiences a drag force. However, this particle moves very slowly, much slower than the local sound speed. As the particle is very massive, it affects its surroundings significantly, for instance by attracting mass. It may therefore be difficult to accurately determine the relative velocity between the particle and its surroundings. We have not made any attempts to calculate the force acting on it.

4.3 The dependence of simulated gravitational drag on resolution

Presumably the difference between lower and higher resolution simulations has something to do with the strength of the interaction which takes place in the vicinity of the planet. It is likely that the strength of the interaction is not well represented, for example, when $R_{\rm A}$ is not well resolved. In our higher resolution simulations $R_{\rm A}$ is a factor of 3–8 smaller than the cell size, while in the lower resolution simulations it is a factor of 5–15 smaller than the cell size (the range is due to the fact that $R_{\rm A}$ varies, while the cell size is fixed). In principle, a convergence test carried out over multiple resolutions with a range of smoothing lengths could identify a problem, but due to the computational expense of these simulations, only limited resolution tests are carried out. When limited tests are carried out several effects can counter each other and confuse the issue of whether the gravitational drag is well represented.

We have performed several test simulations of a point mass moving through a constant density medium in order to eliminate the density gradient, which can complicate matters, and to reduce the computational expense of the tests. In these test simulations we have varied the density, thermal energy (and hence the sound speed), and the particle's velocity. In this way, we have been varying $R_{\rm A}$ so as to make it larger or smaller than the cell size. We found that when $R_{\rm A}$ is underresolved, the drag force acting on the particle in the simulation tends to be overestimated compared to the analytical expression.

Contrary to this expectation, we find that the peak drag force is a factor of ≈2 *higher* in the high-resolution simulations than in the low-resolution simulations. It is possible that this may be due to the density structure of the 1D MESA model in the 3D grid being more compact and have higher density in the higher resolution (Fig. 4, fifth panel from the top), compared to the lower resolution simulations. The more compact and dense giant star in the higher resolution simulation means that not only the peak drag force, but the drag force acting on the planet in general is larger than at lower resolution. This may make up for the possible force underestimation due to not resolving R_A.

5 DISCUSSION

5.1 The intensity, time-scale and frequency of planet merger transients

We start by examining the interaction time-scales. We find that the planet in-spirals relatively fast (few years for RGB stars and ~100 yr for the AGB case), although this is slow compared to CE interactions with more massive companions (e.g. De Marco et al. 2012; Passy et al. 2012a; Ricker & Taam 2012). The hydrodynamic drag was not modelled, but we found that it could play a role at the end of the RGB interaction and this could shorten the in-spiral time-scale somewhat. Pre-empting our discussion in Section 5.2, the planet will be eventually destroyed on a time-scale that is likely of the same order of magnitude as the one characterizing the initial in-spiral.

During the time of the in-spiral, the photosphere expands and the star likely brightens. Using the values of the density at the photosphere from the MESA models (≈9×10^{-9} and 1.6×10^{-9} g cm^{-3} for the RGB and AGB stars, respectively), we find that the interaction with the planet has caused the RGB star to expand by ≈40 per cent over 3 yr, and the AGB star to expand by ≈20 per cent over 80 yr. If the temperature of the photosphere remains constant, this would indicate a modest increase in luminosity by a factor of 2 for the RGB star, and ≈40 per cent for the AGB star. The temperature however, may decreases somewhat, as is demonstrated by Mira stars that can double their radius and halve their effective temperature over pulsation cycles of a few ×100 d (e.g. *o* Cet; Ireland, Scholz & Wood 2008, 2011). Additional cooling of the photosphere may be expected in the case of the AGB star. If we accounted for a decreasing temperature linearly inverse to the increase in radius then the luminosity would actually drop. It is possible, on the other hand, that the photosphere would be farther out than we have considered because of the low-density material that readily expands out. Unfortunately we cannot integrate the optical depth of the material because its temperature is affected by the artificially large 'vacuum' temperature used in ENZO, making these tenuous outer layers more optically thick than they should be.

The average thermal time-scales of the stars are 7600 and 30 yr for the RGB and AGB stars, respectively. The RGB simulation ends at ≈4 $R_\odot$, and this is likely an upper limit. It is entirely possible that with a higher resolution, the 'destruction depth' of ~1 $R_\odot$ (Section 5.2) would be reached within similar time-scales. For the AGB star this is less likely. However its thermal time-scale is much shorter and of the order of the in-spiral time-scale. It is therefore possible that the AGB star would contract on the same time-scales as it is expanding because of the injected orbital energy. If this happened, it is likely that the in-spiral would continue. We posit therefore that both interactions would result in the planet destruction within a time-scale that is of the same order of magnitude of the in-spiral time-scale.

Assuming that there are 10^{10} stars in the Galaxy that are able to evolve off the main sequence over the age of the Universe, and that they have an average lifetime of 10 billion years, then we would have 10^7 RGB and 10^6 AGB stars at any given time in the Galaxy (using RGB and AGB lifetimes of 10 and 1 million years, respectively – see Moe & De Marco 2006 for references to this back of the envelope calculation). Given the planet-swallowing time-scales determined in this work, this would mean that one RGB star in a million would be undergoing an interaction with a companion if all RGB star went through one such interaction in their lives. For the AGB, it would be one star in 10 000 if they too went through one such interaction in their lives. This would mean that 10 RGB stars and 100 AGB stars in the Galaxy would be going through such interaction at any one time. These predictions are similar to what could be surmised by the considerations of Metzger et al. (2012) who discuss that the rate of planet–main-sequence star merger should be similar to the rate of planet–giant star merger, both approximately a few per year.

Given the long brightening and dimming time-scales (relatively to any survey time-scale) and the relatively small variation amplitude predicted, these phenomena may not be observable, unless a more powerful outburst could be triggered (Soker 1991; Bear, Kashi & Soker 2011). This would be quite different from the case of a planet–main-sequence star merger discussed by Metzger et al. (2012). Alternatively, as discussed in Nordhaus & Blackman (2006), if the planet is tidally disrupted, it can form a disc deep inside the star which can lead to a disc-driven outflow.

Very little mass is unbound from the system. Energy loss due to non-conservation may have decreased the mass-loss rate from the AGB star somewhat, but this could not be said of the RGB star for which the total energy slightly increased due to lack of perfect conservation. Additionally, non-simulated effects that could increase the mass-loss rate may be the interference, particularly for the case of the AGB star, of the orbital period with the fundamental pulsation period of the star. If little or no mass is ejected from the system due to the interaction, it is likely that the stars will settle back into an equilibrium stage after radiating their excess energies over their thermal time-scales of 7600 and 30 yr, for the RGB and AGB stars, respectively.

The interaction caused the puffed-up, low density, outer layers of the star to rotate, with velocities $>20\,\mathrm{km\,s^{-1}}$ in the RGB star and $>5\,\mathrm{km\,s^{-1}}$ in the AGB star (the extra angular momentum transported by a planet captured tidally would only change these values slightly). At higher densities, we found no significant rotation. This could indicate that the differential rotation mediated dynamo effect suggested in Nordhaus & Blackman (2006) will not lead to large-scale outflows. We expect that as the interaction ends and the star settles back into its original configuration, and the angular momentum is redistributed in the star, the surface rotation would slow down. Hence, an apparently relatively fast spinning giant star for a brief period could be an indication of a recent CE interaction between the star and a giant planet.

Carlberg et al. (2009) investigated the ability of planet accretion to spin-up stars, and found that in some cases RGB stars could become rapid rotators due to merger with a companion planet although they found that fast rotation was more likely to be achieved if the planet was captured by a subgiant, as stronger mass-loss from giants can remove angular momentum from the envelope preventing the rapid rotation. If this happened, the giant would be slowly rotating or not rotating at all. Based on our simulations, we suggest that the CE event is still capable of causing a rapid rotation in the outer puffed-up envelope, as the CE interaction is fast and mass-loss therefore cannot remove angular momentum sufficiently fast to prevent the spin-up.

5.2 Destroying planets and polluting giant stars

We assume that at some point the planet will be destroyed in the envelope of the giant star. During the in-spiral there are competing processes that try to disrupt the planet. These act on different time-scales and vary with depth. The planet can be (i) disrupted by shear between its outer layers and the stellar ambient density, (ii) it can he ablated by heating and (iii) it can be tidally disrupted. We find that the planet is stable against Kelvin–Helmholtz and Rayleigh–Taylor instabilities caused by shear (discussed in Passy et al. 2012b) for the conditions prevailing during our simulations. We find that a $10\,M_{\rm J}$ planet will be ablated by heating when the separation between the planet and the core of the giant star is $\sim 1\,\mathrm{R_{\odot}}$ (Soker 1998). This is also the distance from the stellar core at which the planet will overflow its Roche lobe. This is a much smaller separation than the values of 10 and 85 $\mathrm{R_{\odot}}$ reached at the end of our RGB and AGB simulations, respectively. Therefore we presume that this event has not yet taken place, but will in time (a time possibly commensurate with the time for the early in-spiral).

Next we ask whether massive planets such as those we have simulated, once destroyed at $\sim 1\,\mathrm{R_{\odot}}$ can alter the giant composition in an observable way. The masses and compositions of the cores of massive exoplanets are poorly known (especially for hot Jupiters; for a recent review, see Spiegel, Fortney & Sotin 2014). We assume that a $10\,M_{\rm J}$ planet consists mainly of an atmosphere of hydrogen and helium in solar proportions, and of a core with an iron mass of $m_{\rm Fe} = 10\ \mathrm{M_{\oplus}} = 3 \times 10^{-5}\ \mathrm{M_{\odot}}$ (Guillot 1999). The base of the convective region in our MESA RGB model is at $\approx 0.4\,\mathrm{R_{\odot}}$, while for the AGB star it is at $\approx 0.2\,\mathrm{R_{\odot}}$; both are deeper than the location at which we predicted the planet to be destroyed. The disrupted planet mass will therefore quickly be mixed into the giant stars' envelopes due to convection.

In Table 1, we list the RGB and AGB star masses, envelope masses and hydrogen masses for a hydrogen mass fraction of 70 per cent. For a solar metallicity ($\epsilon_{\rm Fe} = 7.47$ for the Sun or $m_{\rm Fe}/m_{\rm H} \approx 0.0017$; Scott et al. 2015), we therefore see that the added iron from the planet increases the envelope metallicity too little to be observed.

If we assumed that the iron mass fraction has to grow by at least a factor of 1.5 to be discerned from the base metallicity of the star, then the base metallicity of the star should be [Fe/H] < -1.7 in the AGB case. A giant with a mass of $\sim 1\ \mathrm{M_{\odot}}$ and an envelope mass of 0.5 $\mathrm{M_{\odot}}$ would enable us to detect the pollution more readily at higher, but still sub-solar metallicities ([Fe/H] < -1.3).

Since there appears to be a correlation between a planet's metal fraction (i.e. core mass in a gas giant) and the metallicity of the host star (Guillot et al. 2006), it may be that such low-metallicity stars cannot harbour metal-rich planets. On the other hand, there may also be considerable variability in the metal content of planets. For instance, the planet HD 149026b is thought to contain 60-93 $\mathrm{M_{\oplus}}$ of heavy elements (Fortney et al. 2006), much more than we have considered above. However, even such large core mass would not be able to noticeably alter the observed metallicity of a solar metallicity star.

Another possibility for getting metal enrichment in AGB stars was discussed by Soker (1992), who studied CE interactions between AGB stars and brown dwarfs, and suggested that for separations between 3–10 $\mathrm{R_{\odot}}$, the brown dwarf would excite gravity waves that could lead to a spin-up of the inner envelope. This could also lead to mixing near the core, causing extra dredge-up of core

Table 1. Increase in the mass fraction of iron assuming that the destroyed planet has a core made of iron with a mass of 10 $\mathrm{M_{\oplus}}$.

	RGB star	AGB star
Mass ($\mathrm{M_{\odot}}$)	3.5	3.0
Envelope mass ($\mathrm{M_{\odot}}$)	3.0	2.5
Hydrogen mass ($\mathrm{M_{\odot}}$)	2.1	1.75
Enrichment@[Fe/H]$_{\odot}$ (per cent)	0.8	1
Enrichment@[Fe/H]$= -1.7$ (per cent)	43	50

material into the envelope. Hence, if this process happened near the last stages of mass-loss, the wind of the AGB star would be enriched in heavier elements. However, this star would be a much more evolved AGB star than the one we have considered in this work, and this mechanism requires that the companion enters the CE only at the very late stages of AGB evolution.

6 SUMMARY

We have simulated the CE interaction between a $10\,M_\mathrm{J}$ planet and a $3.5\ \mathrm{M}_\odot$ RGB star or a $3.05\ \mathrm{M}_\odot$ AGB star using the grid code ENZO with a uniform, cubic grid with a maximum resolution of 512 cells on a side. These simulations have several limitations, but can give order-of-magnitude quantitative information.

The limited resolution in our simulation affects the final separation of our simulations, and some of the results from late times in our simulations may not be accurate. Another effect of the resolution is that the accretion radius is not resolved, which can lead to an overestimate of the force. However, in lower resolution simulations the star diffuses out more leading to lower densities which can cause an underestimate of the force, somewhat counteracting the overestimate from not resolving the accretion radius. Future simulations using an adaptive mesh refinement simulation code, or possibly a smoothed particle hydrodynamics code may be able to overcome some of these limitations. We nevertheless found that:

(i) Plunge-in times of the order of years to decades are seen in our simulations for the RGB and AGB cases, respectively. The plunge-in times of low-mass companions such as planets in the envelopes of giants are relatively longer than for more massive, stellar companions, with the longer times being witnessed for the more evolved, lower density primaries.

(ii) We concluded that the planets should not be disrupted during the simulated phase. We cannot tell with precision how much longer the planets will take to reach a depth where disruption takes place.

(iii) Destroyed planets will pollute the envelopes of giant stars, but the effect is likely to be witnessed only in the lowest mass giants with the lowest metallicity, if these stars can have planets with suitably massive metal cores.

(iv) Only a very small amount of the primary star's envelope mass is unbound by the planet in our simulation. It is possible that if the planet interacts with the star's pulsation this may trigger further unbinding, or, if the planet is tidally disrupted it can form a disc inside the giant star from which a disc-driven outflow can form.

(v) The expanding giant's luminosity may increase by a modest factor over a relatively short time-scale of the early in-spiral (though still long compared to survey time-scales). This effect would likely be relatively rare and difficult to observe.

(vi) In line with other studies, we find that the penetration of the planets into the giants will stimulate faster rotation. However as this rotation is limited to the outer layers, it is not clear in what time-scales the angular momentum will re-distribute into the entire envelope and what the final rotation rate of the giants will be.

(vii) Analytically, it is predicted that the gravitational drag force would peak at the sonic point and greatly diminish for subsonic regimes. In our simulations the slowing down of the in-spiral takes place at such a transition. The overall force experienced by the planets in our simulations is larger than calculated analytically and is larger for higher resolution. This may simply be due to us assuming $\zeta = 1$ in equation (2). It is also possible that the presence of a density gradient may enhance the intensity of the gravitational drag. We leave further comparisons between numerical and analytical gravitational drag to future work.

ACKNOWLEDGEMENTS

We thank the anonymous referee for constructive comments which helped improve the paper. We thank B. Pandey and M. Wardle for constructive discussions during this work, and C. O'Neill for helpful input. JES acknowledges support from the Australian Research Council Discovery Project (DP12013337) programme. OD gratefully acknowledges support from the Australian Research Council Future Fellowship grant FT120100452. J-CP acknowledges funding from the Alexander-von-Humboldt Foundation. This research was undertaken, in part, on the NCI National Facility in Canberra, Australia, which is supported by the Australian Commonwealth Government. Computations described in this work were performed using the ENZO code (http://enzo- project.org), which is the product of a collaborative effort of scientists at many universities and national laboratories.

REFERENCES

Bear E., Kashi A., Soker N., 2011, MNRAS, 416, 1965
Beuermann K. et al., 2011, A&A, 526, 53
Bondi H., 1952, MNRAS, 114, 195
Bryan G. et al., 2014, ApJS, 211, 19
Carlberg J. K., Majewski S. R., Arras P., 2009, ApJ, 700, 832
Charpinet S. et al., 2011, Nature, 480, 496
De Marco O., Passy J. C., Moe M., Herwig F., Mac Low M.-M., Paxton B., 2011, MNRAS, 411, 2277
De Marco O., Passy J.-C., Herwig F., Fryer C. L., Mac Low M.-M., Oishi J. S., 2012, in Richards M. T., Hubeny I., eds, Proc. IAU Symp. 282, From Interacting Binaries to Exoplanets: Essential Modeling Tools. Cambridge Univ. Press, Cambridge, p. 517
Fortney J. J., Saumon D., Marley M. S., Lodders K., Freedman R. S., 2006, ApJ, 642, 495
Guillot T., 1999, Science, 286, 72
Guillot T., Santos N. C., Pont F., Iro N., Melo C., Ribas I., 2006, A&A, 453, L21
Horner J., Wittenmyer R. A., Hinse T. C., Marshall J. P., Mustill A. J. Tinney C. G., 2013, MNRAS, 435, 2033
Hoyle F., Lyttleton R. A., 1939, Proc. Camb. Phil. Soc., 35, 405
Iben I., Jr, Livio M., 1993, PASP, 105, 1373
Ireland M. J., Scholz M., Wood P. R., 2008, MNRAS, 391, 1994
Ireland M. J., Scholz M., Wood P. R., 2011, MNRAS, 418, 114
Ivanova N. et al., 2013, A&AR, 21, 59
MacLeod M., Ramirez-Ruiz E., 2015, ApJ, 803, 41
Metzger B. D., Giannios D., Spiegel D. S., 2012, MNRAS, 425, 2778
Moe M., De Marco O., 2006, ApJ, 650, 916
Mustill A. J., Villaver E., 2012, ApJ, 761, 121
Nandez J. L. A., Ivanova N., Lombardi J. C., 2015, MNRAS, 450, L39
Nelemans G., Tauris T. M., 1998, A&A, 335, L85
Nordhaus J., Blackman E. G., 2006, MNRAS, 370, 2004
Nordhaus J., Spiegel D. S., 2013, MNRAS, 432, 500
O'Shea B. W., Bryan G., Bordner J., Norman M. L., Abel T., Harkness R., Kritsuk A., 2004, preprint (astro-ph/0403044)
Ostriker E. C., 1999, ApJ, 513, 252
Paczynski B., 1976, in Eggleton P., Mitton S., Whelan J., eds, Proc. IAU Symp. 73, Structure and Evolution of Close Binary Systems. Reidel, Dordrecht, p. 75
Parsons S. G. et al., 2014, MNRAS, 438, 91
Passy J. C. et al., 2012a, ApJ, 744, 52
Passy J. C., Mac Low M.-M., De Marco O., 2012b, ApJ, 759, L30
Paxton B., Bildsten L., Dotter A., Herwig F., Lesaffre P., Timmes F., 2011, ApJS, 192, 3
Paxton B. et al., 2013, ApJS, 208, 4

Ricker P. M., Taam R. E., 2008, ApJ, 672, 41

Ricker P. M., Taam R. E., 2012, ApJ, 746, 74

Sandquist E. L., Taam R. E., Chen X., Bodenheimer P., Burkert A., 1998, ApJ, 500, 909

Scott P., Asplund M., Grevesse N., Bergemann M., Sauval J., 2015, A&A, 573, 26

Setiawan J., Klement R. J., Henning T., Rix H.-W., Rochau B., Rodmann J., Schulze-Hartung T., 2010, Science, 330, 1642

Shima E., Matsuda H., Sawada K., 1985, MNRAS, 217, 367

Silvotti R. et al., 2014, A&A, 570, 130

Soker N., 1991, ApJ, 367, 593

Soker N., 1992, ApJ, 399, 185

Soker N., 1998, AJ, 116, 1308

Spiegel D. S., Fortney J. J., Sotin C., 2014, PNAS, 111, 12622

Staff J. E., De Marco O., Macdonald Evans D., Galaviz P., Passy J.-C., 2016, MNRAS, 455, 3511

Udry S., Santos N., 2007, ARA&A, 45, 397

Villaver E., Livio M., 2007, ApJ, 661, 1192

Villaver E., Livio M., 2009, ApJ, 705, 81

Wolszczan A. Frail D. A., 1992, Nature, 355, 145

APPENDIX A: FITTING RESULTS

For both of the simulations, we fit the planet's velocity and the planet's total energy, to get smooth curves. We have not attempted to estimate the χ^2 of the fits. Instead, we have shown in Fig. 7 the data and the fitted curves from the low-resolution simulations, and limit ourself to stating that qualitatively the fits look reasonable. In this appendix, we show the details of the fits and the results for the two low-resolution simulations.

A1 RGB case

We fit the planet's velocity with a fifth-order polynomial ($ax^5 + bx^4 + cx^3 + dx^2 + ex + f$) over the entire data-range from 0 to 980 d. The result of the fit is: $a = 9.850\,28 \times 10^{-8}$, $b = -0.000\,237$, $c = 0.188\,86$, $d = -56.0575$, $e = 7229.48$ and $f = 1.041\,92 \times 10^7$. The planet's negative total energy was fitted with two different curves. To ensure a reasonably continuous fit with a reasonably continuous first derivative, we fit the curves over a larger range than we plot them. From 0 to 560 d, we use a third-order polynomial ($f_1(x) = a_1x^3 + b_1x^2 + c_1x + d_1$) where we found the coefficients to be $a_1 = 1.932\,53 \times 10^{36}$, $b_1 = 3.2207 \times 10^{38}$, $c_1 = 2.288\,98 \times 10^{39}$ and $d_1 = 1.070\,75 \times 10^{45}$. This was used to plot the curve from 0 to 510 d. Then from 400 to 980 d, we used a sixth-order polynomial ($f_2(x) = a_2x^6 + b_2x^5 + c_2x^4 + d_2x^3 + e_2x^2 + f_2x + g_2$), where we found the coefficients to be $a_2 = 4.216\,65 \times 10^{30}$, $b_2 = -1.733\,93 \times 10^{34}$, $c_2 = 2.898\,79 \times 10^{37}$, $d_2 = -2.519\,62 \times 10^{40}$, $e_2 = 1.201\,86 \times 10^{43}$, $f_2 = -2.985\,64 \times 10^{45}$ and $g_2 = 3.033\,51 \times 10^{47}$. This was plot from 510 to 980 d.

A2 AGB case

We fit the planet's velocity to a fifth-order polynomial ($ax^5 + bx^4 + cx^3 + dx^2 + ex + f$) over the entire data-range from 0 to 77.5 yr. The result of the fit is: $a = 0.008\,323\,47$, $b = -1.525\,15$, $c = 96.5916$, $d = -2287.46$, $e = 22\,336.7$, and $f = 3.350\,88 \times 10^6$, with 150 deg of freedom. The planet's negative total energy we fit with three different curves. To ensure a reasonably continuous fit with a reasonably continuous first derivative, we fit the curves over a larger range than we plot them. From 0 to 35 yr, we fit a first-order polynomial ($f_1(x) = ax + b$) and results in $a = 5.286\,12 \times 10^{41}$ and $b = 1.055\,81 \times 10^{44}$. This we used to plot from 0 to 27 yr. From 5 to 70 yr, we fit a sixth-order polynomial ($f_2(x) = ax^6 + bx^5 + cx^4 + dx^3 + ex^2 + fx + g$) which results in $a = -1.223\,17 \times 10^{35}$, $b = 2.120\,89 \times 10^{37}$, $c = -1.303\,96 \times 10^{39}$, $d = 3.642\,03 \times 10^{40}$, $e = -4.515\,27 \times 10^{41}$, $f = 2.242\,52 \times 10^{42}$ and $g = 1.073\,88 \times 10^{44}$, which was plotted from 27 to 55.5 yr. Finally, from 45 to 77.5 yr, we fit an eighth-order polynomial ($f_3(x) = ax^8 + bx^7 + cx^6 + dx^5 + ex^4 + fx^3 + gx^2 + hx + i$), which was fitted from 45 to 77.5 yr and results in: $a = 3.457\,42 \times 10^{31}$, $b = -8.186\,03 \times 10^{33}$, $c = 7.092\,31 \times 10^{31}$, $d = -2.719\,83 \times 10^{37}$, $e = 4.273\,98 \times 10^{38}$, $f = 5.972\,99 \times 10^{22}$, $g = 1.122\,44 \times 10^{21}$, $h = 2.261\,62 \times 10^{19}$, $i = 1.243\,44 \times 10^{16}$. This was plotted from 55.5 to 77.5 yr.

This paper has been typeset from a TEX/LATEX file prepared by the author.